U$_{1.33}$T$_4$Al$_8$Si$_2$ (T = Ni, Co): Complex Uranium Silicides Grown from Aluminum/Gallium Flux Mixtures

Ashini S. Jayasinghe,[†] You Lai,[‡] Ryan Baumbach,[‡] and Susan E. Latturner[*,†]

[†]Department of Chemistry and Biochemistry, Florida State University, Tallahassee, Florida 32306, United States

[‡]Department of Physics, Florida State University and National High Magnetic Field Laboratory, Tallahassee, Florida 32310, United States

S *Supporting Information*

ABSTRACT: Two new quaternary analogs of the Gd$_{1+x}$Fe$_4$Si$_{10-y}$ structure type were grown from the reaction of uranium, silicon, and a transition metal (nickel or cobalt) in an excess of aluminum/gallium flux. The use of a mixed flux was found to be necessary for the formation of U$_{1.33}$T$_4$Al$_8$Si$_2$ (T = Ni, Co). Single crystal X-ray diffraction data shows the presence of disordered U/Si layers that are characteristic of this structure type; precession photographs indicate partial formation of a superstructure and stacking disorder along the *c*-axis. This disorder may be the cause of the spin glass behavior that is particularly evident in the nickel analog, which exhibits a spin freezing transition at T_F = 7 K. These compounds are resistant to chemical attack and oxidation and may be potential waste forms.
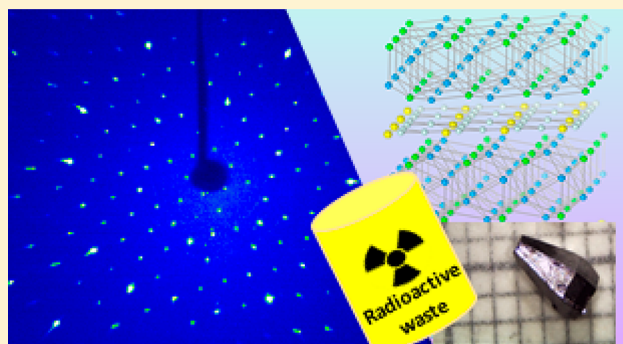
INTRODUCTION

Electricity has become a vital part of modern life, and around 20% of U.S. energy demand is supplied by nuclear reactors.[1−3] However, this leads to the generation of large quantities of radioactive waste; there are roughly 300 million L of radioactive waste in underground tanks at the Savannah River and Hanford sites alone.[2,4] This necessitates research into effective waste storage methods and creation of stable, storable actinide compounds.[4] Due to their high stability and refractory properties, uranium silicides are potential candidates for radioactive waste storage.[5−7] While silicides of transition metals and lanthanides are very well investigated, complex actinide silicides have been scarcely explored.[8−11] The study of the properties of multinary uranium silicide materials is vital to advancing the knowledge base of these compounds. In addition to their refractory properties, these compounds may also exhibit unusual magnetic behavior. This is particularly likely for those that also contain transition metals; coupling of delocalized d-orbitals with relatively localized f-orbitals of uranium can lead to exotic magnetic phenomena such as spin glass behavior, superconductivity, heavy fermion behavior, and the Kondo effect.[12−17]

The growth of materials as single crystals greatly facilitates characterization of structural and electronic properties. Traditional solid-state synthesis typically requires temperatures over 1000 °C and often results in polycrystalline products. Flux synthesis using a large excess of molten metal (or a mixture of metals) as a reaction medium has proven to be an effective method to synthesize novel metal silicide single crystals. This

technique allows for lower reaction temperatures, enabling isolation of complex kinetically stabilized products instead of the most commonly formed thermodynamically stable products.[18−21] This is exemplified by the growth of quaternary Th$_2$(Au$_x$Si$_{1−x}$)[AuAl$_2$]$_n$Si$_2$ (n = 1, 2, 4)[22] and RE$_{0.67}$T$_2$Ga$_{5-x}$Tt$_x$ (RE = Y, Sm, Gd−Tm; T = Ni, Co; Tt = Si, Ge)[23] crystals in Al and Ga flux, respectively.

In this work two new U$_{1.33}$T$_4$Al$_8$Si$_2$ (T = Ni/Co) compounds were synthesized in aluminum/gallium flux mixtures. These phases form in the Gd$_{1+x}$Fe$_4$Si$_{10-y}$ structure type and exhibit the structural disorder that is inherent to this family of compounds.[23−28] Both compounds are stable to water, brine solutions, and heating in air up to 900 °C. Magnetic susceptibility measurements on single crystals reveal anisotropic Curie−Weiss behavior at elevated temperatures, indicating that the uranium ions carry an f-moment. Magnetic transitions are observed for both compounds at low temperatures, with the Co analog exhibiting fragile antiferromagnetism below 5 K. The Ni analog exhibits more complex behavior suggestive of spin frustration or glassy magnetism below 7 K. Heat capacity data for both compounds feature an enhanced electronic coefficient of the heat capacity at low temperature which relates to Kondo hybridization between the f- and conduction electron states. Finally, both compounds exhibit weak temperature dependences of the electrical resistivity that

Table 1. Selected Crystallographic Data for $U_{1.33}T_4Al_8Si_2$ Crystals

formula[a]	$U_{1.05(1)}Ni_4Al_{7.72(4)}Si_{1.80(4)}Ga_{0.48(6)}$	$U_{1.36(1)}Co_4Al_{7.80(3)}Si_{1.91(4)}Ga_{0.20(4)}$
formula weight	777.51	827.43
space group	hexagonal, $P6_3/mmc$	hexagonal, $P6_3/mmc$
unit cell dimensions (Å)	$a = 4.1246(7)$; $c = 15.735(4)$	$a = 4.0480(6)$ $c = 15.663(3)$
volume (Å^3)	231.83(10)	222.27(8)
Z	1	1
ρ_{calc} (g/cm^3)	5.57	6.26
μ (mm^{-1})	28.54	33.54
F(000)	349	367
crystal size (μm)	$80 \times 40 \times 10$	$40 \times 40 \times 20$
θ range for data collection (deg)	2.589 to 34.212	2.601 to 32.098
limiting indices	$-6 \leq h \leq 6, -6 \leq k \leq 6, -24 \leq l \leq 24$	$-6 \leq h \leq 6, -5 \leq k \leq 6, -23 \leq l \leq 20$
reflections collected/unique	4603/228 [R(int) = 0.0531]	3142/188 [R(int) = 0.0353]
GOF	1.171	1.123
final R indices [$I > 2\sigma(I)$]	R1 = 0.0277; wR2 = 0.0778	R1 = 0.0180, wR2 = 0.0489
R indices (all data)	R1 = 0.0279; wR2 = 0.0780	R1 = 0.0180 wR2 = 0.0489
largest diff. peak and hole	4.977 and -1.812	0.865 and -0.946

[a]The idealized formula $U_{1.33}T_4Al_8Si_2$ is used in the text for conciseness.

originate from strong disorder scattering of the conduction electrons.

EXPERIMENTAL PROCEDURE

Synthesis. *Caution! U metal used in the reactions contains radioactive ^{238}U, which is an α-emitter, and like all radioactive materials, it must be handled with care. These experiments were conducted by trained personnel in a licensed research facility with special precautions taken toward the handling, monitoring, and disposal of radioactive materials.*

Uranium pieces (Johnson Matthey, 99.8%), transition metal slugs (T = Co or Ni; Alfa Aesar, 99.95 and 99.98% respectively), and silicon wafer pieces (99.999%) were arc-melted in a 0.5:1:1 U/T/Si molar ratio in a MAM-1 compact arc melter under an atmosphere of Ar gas. The arc melted pellets were broken into pieces and sufficient quantities weighed out to provide the three elements in 0.5, 1, and 1 mmol amounts which were placed in alumina crucibles and combined with 10 mmol of aluminum (slugs, Alfa Aesar, 99.99%) and 10 mmol of gallium (pieces, Alfa Aesar, 99.99%). The crucibles were placed in quartz sleeves along with silica wool on top to act as a filter and sealed under vacuum. Then the sealed tubes were heated to 1000 °C in 12 h and maintained at that temperature for 24 h, then cooled to 800 °C in 60 h. The reaction ampules were taken out of the furnace, inverted, and centrifuged to separate excess flux from the product crystals. In order to investigate the impact of Al and Ga concentrations, the same experiments were repeated using Al:Ga mmol ratios of 10:5 and 15:5. Also, to confirm the importance of the initial arc melting of uranium with transition metal and silicon, the same experiments were conducted using the individual elemental reactants.

Elemental Analysis. Semiquantitative elemental analysis data were obtained using an FEI NOVA 400 scanning electron microscope (SEM) coupled with energy dispersive X-ray spectroscopy (EDS). Selected crystals were cleaved to expose their interior regions to eliminate erroneous analyses due to flux residue that can be present on the surface. Sample surfaces were oriented on carbon tape perpendicular to the electron beam. The crystals were analyzed using a 30 kV accelerating voltage and an accumulation time of 50 s. To confirm the elemental composition of all the crystals is similar, at least 20 crystals of each compound were analyzed.

Structural Analysis. Smaller pieces cleaved from single crystals were coated in oil, placed in MiTeGen mounts and mounted on a Bruker D8 Quest single-crystal X-ray diffractometer equipped with Mo Kα radiation ($\lambda = 0.7107$ Å). Data were collected at room temperature with the Bruker software package,[29] and peak intensities were corrected for Lorentz, polarization, and background effects using the Bruker APEX III software.[30] An empirical absorption correction

was applied using the program SADABS, and the structure solution was determined by intrinsic phasing methods and refined on the basis of F2 for all unique data using the SHELXTL program suite.[31] Aluminum and silicon are indistinguishable in X-ray diffraction experiments, so light element sites in the structure were assigned as either Al or Si based on bond lengths to neighboring atoms and consideration of the Al/Si ratios observed in the elemental analysis of samples (see Results and Discussion). X-ray diffraction precession images of h0l and hk0 zones were collected on $U_{1.33}T_4Al_8Si_2$ crystals with 100 s exposure time. Some crystallographic data are given in Table 1.

Powder X-ray Diffraction. The purity of the bulk materials was confirmed using powder X-ray diffraction (PXRD) experiments. Diffractograms were collected from 10 to 80° in 2θ with a step size of 0.017 on a PANalytical X-Pert PRO instrument using Cu Kα radiation. The samples were prepared by grinding the crystalline product using a mortar and pestle under acetone and the powder deposited on PANalytical sample holders.

Chemical and Thermal Stability. To determine the stability of these materials in different media, crystals were immersed in water and 1 M HCl, 1 M HNO$_3$, 6 M NaOH, and 10 wt % brine solutions. These crystals were observed after 1 day, 4 days, and 1, 2, 4, and 6 weeks to observe if there were any changes in appearance, and then X-ray diffraction data were collected to confirm the structural integrity. Thermogravimetric analyses of the $U_{1.33}T_4Al_8Si_2$ samples were conducted with a SDT Q600 from TA Instruments. Crystals were loaded into alumina pans and samples were heated up to 900 °C at a ramp rate of 5 °C per minute under flowing air (100 mL/min).

Magnetic and Electronic Properties Measurements. Measurements of the magnetization were performed on oriented crystals of the title phases using a Quantum Design MPMS3 magnetometer. The temperature-dependent DC magnetic susceptibility data $\chi = M/H$ were measured between $T = 1.8-300$ K using applied fields $H = 100$ and 1000 Oe; field dependent magnetization data $M(H)$ were collected at $T = 1.8$ K for $H < 7$ T, respectively. AC magnetic susceptibility measurements were performed for $U_{1.33}Ni_4Al_8Si_2$ at $T < 15$ K, with $H \perp c$, $H = 1$ Oe and frequencies at 7.57, 75.7, and 757 Hz. Heat capacity data were measured using the standard relaxation technique in a Quantum Design Physical Properties Measurement System at $T = 0.4-50$ K in zero magnetic field. The electrical resistivity was measured using a standard four contact technique for $T = 1.8-300$ K using a QD-PPMS.

RESULTS AND DISCUSSION

Reactions of U/Ni/Si and U/Co/Si mixtures in aluminum/ gallium flux produce silver crystals of $U_{1.33}T_4Al_8Si_2$ (T = Ni or

Co) with 40% and 45% yields (based on uranium), respectively. These faceted rod crystals have a hexagonal cross-section and consistently feature tapered pointed ends resulting in a "pencil shape" as shown in Figure 1. This distinct
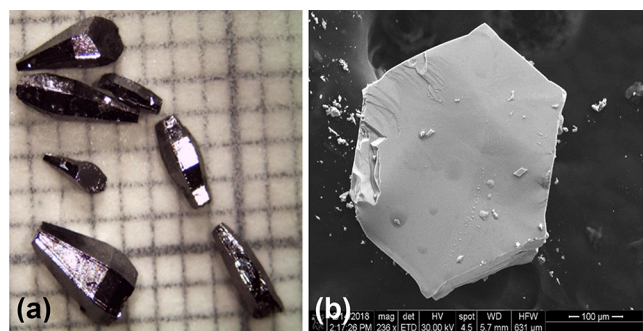
Figure 1. (a) Microscope image of pencil-shaped $U_{1.33}Ni_4Al_8Si_2$ crystals on mm grid paper. (b) SEM image of a hexagonal cross section of a $U_{1.33}Ni_4Al_8Si_2$ crystal

pencil shape was also observed in other ternary and quaternary R/T/M/M′ analogs (R = rare earth, T = transition metal, M/ M′ = main group elements) reported in the literature with the $Gd_{1+x}Fe_4Si_{10-y}$ structure type.[23,24,26] In reactions containing cobalt, the only product observed was $U_{1.33}Co_4Al_8Si_2$. However, the reactions containing nickel yielded two products, with easily distinguishable crystal habits. Besides the pencil-shaped $U_{1.33}Ni_4Al_8Si_2$ phase, cubic shaped crystals shown in Figure S1 (Supporting Information) were also formed with around 15% yield. Preliminary analysis indicates that this cubic phase product is likely a gallium and silicon-substituted variant of UAl_3. This was confirmed with PXRD data on the products, which displayed the presence of $U_{1.33}Ni_4Al_8Si_2$ and UAl_xSi_{3-x} (Figure S2). In contrast, for the $U_{1.33}Co_4Al_8Si_2$ sample, the PXRD powder pattern showed a pure phase (Figure S3). Similar reactions were attempted for U/Fe/Si systems and it did not produce the Fe analog of $U_{1.33}T_4Al_8Si_2$ crystals. Instead, gallium-substituted $FeAl_3$ crystals were formed. However, a reaction done in Ga flux with U, Fe, and Si in 0.5, 1, and 6 mmol respectively formed crystals of the previously reported $U_{1.2}Fe_4Si_{9.7}$.[25]

It is notable that the $U_{1.33}T_4Al_8Si_2$ phases are not produced from reactions in either aluminum flux or gallium flux; a mixture of both these elements is required. Reactions of U/T/ Si in aluminum flux produces only cubic $U(Al/Si)_3$; reactions in gallium yield the orthorhombic $UNiSi_2$ phase ($CeNiSi_2$ structure type), $CoGa_3$, and tetragonal UCo_2Si_2 ($ThCr_2Si_2$ structure type). To understand the effect of Al and Ga concentrations in the mixed flux, experiments were repeated with Al: Ga ratios of 1:1, 2:1, and 3:1, while holding all the other factors constant. For the reactions with Co, changing the Al:Ga ratio did not have an impact. However, for the Ni reactions, increasing the Al content favored the formation of cubic $U(Al/Si)_3$ crystals instead of the pencil-shaped $U_{1.33}Ni_4Al_8Si_2$ crystals. Thus, for the synthesis of $U_{1.33}T_4Al_8Si_2$ crystals, using a 1:1 ratio of Al:Ga provides optimal results. Preliminary experiments in Al/Zn flux (2:10 mol ratio) indicate that the same U:Ni:Si, 0.5:1:1 arc-melted reaction mixture occasionally forms $U_{1.33}Ni_4Al_8Si_2$ crystals, but the yield is lower.

If U, T, and Si powders are used as reactants instead of the prearc melted mixture, the reaction in Al/Ga flux does not yield the title phases. Reactions with nickel powder produce prism crystals, subsequently identified as Ni_2Al_3. Similar reactions using cobalt yielded $UCoGa_5$ and Si crystals. Therefore, it can be assumed that pre-arc melting is a necessity to form the $U_{1.33}T_4Al_8Si_2$ compounds. This premixing may prevent the preferential scavenging of one element by the flux (for instance, Ni_2Al_3 and Ni_2Ga_3 form very readily and may remove nickel from the reaction mixture, preventing formation of the desired quaternary product).

Elemental Analysis. The elemental compositions of the products were analyzed using semiquantitative SEM-EDS. The analyses showed the presence of U, T, Si, Al and a small amount of Ga in the pencil-shaped crystals. The average atomic percentages for U:T:Si:Al:Ga were 7(1):31(4):16(2):41(4):5(1) and 10(1):25(5):19(3):39(4):7(2) for the nickel and cobalt analogs, respectively. The cubic crystals observed as by-products in the nickel-containing reactions had U:Si:Al:Ga in 23:23:26:38 atomic ratios, in agreement with this compound being U(Al/Ga/Si)$_3$, a substituted variant of UAl_3 with the cubic $AuCu_3$ structure type.

Stability. Both $U_{1.33}T_4Al_8Si_2$ phases are stable to air and are unreactive to water and 10 wt % brine solutions. Radiological testing of the water and brine solutions after 14 days (using a Tri-Carb 2900TR liquid scintillation analyzer and a Ludlum model 2929 alpha-beta counter) indicated no leaching of uranium into the solutions. The compounds are stable to 6 M NaOH solution for a month, although they show signs of reaction and loss of crystallinity after around 6 weeks. Both $U_{1.33}Ni_4Al_8Si_2$ and $U_{1.33}Co_4Al_8Si_2$ crystals dissolved in 1 M HNO_3 solution within 4 days. However, in 1 M HCl solution, while $U_{1.33}Co_4Al_8Si_2$ crystals again dissolve within 4 days, $U_{1.33}Ni_4Al_8Si_2$ crystals are stable up to 1 month, maintaining their crystallinity although a slight amount of leaching of uranium into the acid solution is indicated. This indicates that the physical properties of the material can be fine-tuned by changing the transition metals.

Heating $U_{1.33}Ni_4Al_8Si_2$ crystals up to 900 °C in air does not result in any significant weight change, as shown in Figure 2. This indicates that the crystals do not decompose or oxidize with elevated temperature. A shiny black coating was observed on the crystals after being heated, which could be removed using a razor blade. SEM/EDS data on this coating showed O, Al, Si, Ni, Ga, and U atomic percentages of 55(7), 26(2), 5(2),
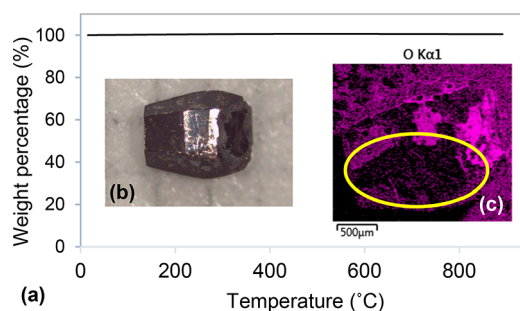
Figure 2. (a) Thermogravimetric analysis of $U_{1.33}Ni_4Al_8Si_2$ compound confirms the structure has stability at high temperatures. (b) Post TGA crystals had a black coating on the surface. (c) A small piece was chipped from the crystal and surface, and the interior of the crystal was compared using SEM-EDS. The circled area shows the inside of the crystal, and the absence of oxygen there confirms the oxidation is confined to the surface of the crystal.

10(2), 1(1), 2.5(0.5)%, respectively, indicating it is an (Al/Ni)$_x$O$_y$ film. When these crystals were cleaved and the inner portions analyzed using SEM/EDS, the O, Al, Si, Ni, Ga, and U atomic percentages were 1.7(0.5), 48(1), 16.1(0.2), 23(1), 4.2(0.1), and 6.85(0.07)% respectively and the complete element map is displayed in Figure S4. This indicates that the oxidation was restricted to the surface of the crystals. Similar results were observed for U$_{1.33}$Co$_4$Al$_8$Si$_2$ crystals (Figure S5)—they did not display a significant weight loss and post-TGA crystals were covered with a black oxide coating. The single crystal data collected on these crystals confirmed that no structural changes had occurred. Similar formation of a protective surface oxide layer was reported by Sieve et al. for REFe$_4$Al$_9$Si$_6$ (RE = Tb, Er) crystals which displayed resistance to oxidation up to 900 °C.[32]

Structure. U$_{1.33}$T$_4$Al$_8$Si$_2$ (T = Co or Ni) has the Gd$_{1+x}$Fe$_4$Si$_{10-y}$ structure type in hexagonal space group $P6_3/mmc$; see Figure 3. Isostructural compounds have been
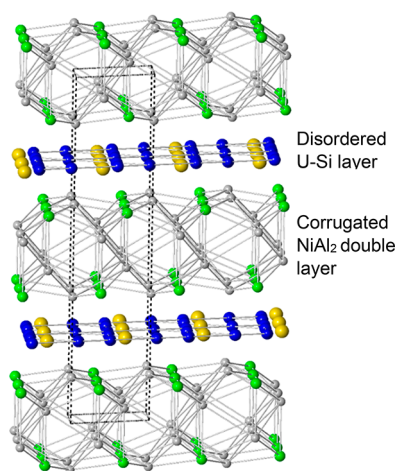

Figure 3. Extended structure of U$_{1.33}$T$_4$Al$_8$Si$_2$ crystal viewed along *a*-axis; for clarity the bonds between the layers are not depicted. U, T, Si, and Al are depicted as yellow, green, blue, and gray spheres, respectively.

reported as R$_{0.67}$T$_2$(M,M′)$_5$, R$_{1.33}$T$_4$M$_{10}$, or R$_2$T$_6$M$_{15}$ (with Z = 2, 1, and $^2/_3$ formula units per unit cell respectively); these varying formulas reflect the inherent disorder and associated variation in stoichiometry of this structure type.[20−22] The ICSD database refers to analogs as possessing either the Y$_2$Fe$_4$Si$_9$ type or Gd$_{1+x}$Fe$_4$Si$_{10-y}$ structure types. These are the Z = 1 stoichiometries; the former structure is one of the earliest reports that did not take into account partial occupancies (see below).

Before further discussion on the structure, it must be pointed out that the similar size and electron count of aluminum and silicon makes assigning the light atom positions using single-crystal X-ray diffraction challenging. In this work, the atom assignments in the crystallographic analysis were done based on the bond distances and SEM/EDS data (Table S1). The observed bond distances were compared to those in other aluminum-silicide intermetallic materials reported in the literature. In accordance with the relative covalent radii of Al and Si (1.25 and 1.17 Å respectively), Si−X bond lengths are often shorter than Al−X bond lengths. Therefore, comparison of observed bond lengths in R/Al/Si intermetallics is often used to assign aluminum and silicon sites in the structure. Several studies that made use of neutron diffraction experiments observed that atom assignment based on bond lengths is accurate for most scenarios; this was seen for compounds such as U$_8$Al$_{19}$Si$_6$, Ho$_2$Al$_3$Si$_2$, and Pr$_8$Ru$_{12}$Al$_{49}$Si$_9$(Al$_x$Si$_{12-x}$).[33−35] The SEM/EDS analyses on the U$_{1.33}$T$_4$Al$_8$Si$_2$ phases show uranium and transition metal percentages that agree well with the atomic percentages indicated by the structure refinement. However, SEM/EDS indicates a somewhat lower Al content and higher Si content than is modeled by the single crystal analysis (see Supporting Information). So there is a possibility that some of the Al sites have Si mixing and vice versa. However, SEM/EDS is semiquantitative. In order to unambiguously assign atom positions, neutron diffraction data are required, and it will be interesting to explore this further in a future study.

This structure is comprised of two building blocks: corrugated NiAl$_2$ double layers separated by U/Si disordered sheets. The NiAl$_2$ corrugated layer can be described as a "stuffed" arsenic type moiety. Two NiAl$_2$ layers are linked together to form the Ni$_2$Al$_4$ slabs in the structure. The Ni−Al distances range from 2.4087(5) to 2.5843(10) Å and Al−Al distances range from 2.7451(15) to 2.801(2) Å. The Ni site is also coordinated to the Si atoms in the U−Si layer with a Ni−Si bond distance of 2.397(3) Å although these bonds are not drawn in Figure 3 to emphasize the 2-D nature of the building blocks. ErNi$_3$Al$_9$ has a similar coordination environment around Ni, with Al−Al bond distances ranging from 2.641 to 2.880 Å and Ni−Al bond distances of 2.305−2.839 Å.[36] In the Sm$_2$Ni$_{3+x}$Si$_{5-x}$ structure reported by Zhuravleva et al., the Ni−Si bond distance range from 2.299 to 2.3685 Å, and the Si−Si bond distance is 2.8484 Å.[37] Selected bond lengths for both U$_{1.33}$T$_4$Al$_8$Si$_2$ analogs are given in Table S1 in the Supporting Information. Elemental analysis showed slight incorporation of Ga in the crystals; some gallium substitution on the aluminum sites is possible. During refinements of the occupancies of the two aluminum sites, the Al2 site did not vary, but the Al1 site (the outermost site of the Ni$_2$Al$_4$ slab) indicated higher than
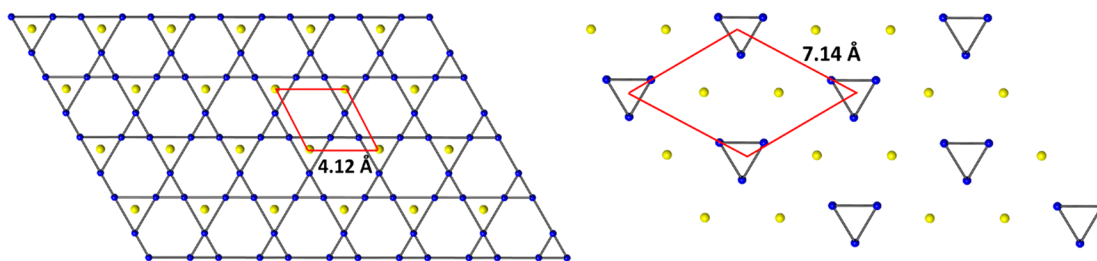
Figure 4. (a) U−Si layer modeled as if all the sites are completely occupied viewed along the *c*-axis. (b) Supercell structure resulting from ordered partial occupancy of the uranium and silicon sites.
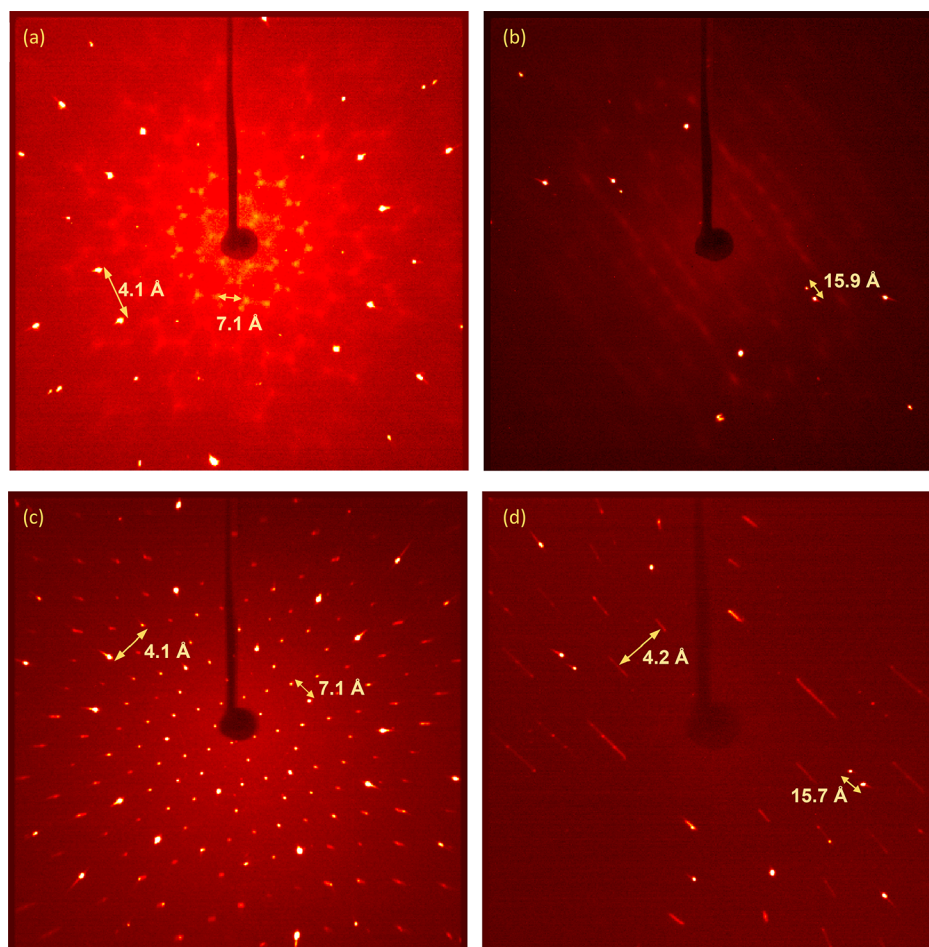
Figure 5. Zone photos collected on crystals of $U_{1.33}T_4Al_8Si_2$: (a) $hk0$ and (b) $0kl$ for $U_{1.33}Ni_4Al_8Si_2$; (c) $hk0$ and (d) $0kl$ for $U_{1.33}Co_4Al_8Si_2$.

100% occupancy. This was subsequently refined as a mixture of 92.8(9)% Al and 7.2(9)% Ga.

The monatomic-thick 2-D layers of uranium/silicon in the structure exhibit partially occupied sites and stacking faults. If the sites in this layer are refined as completely occupied as shown in Figure 4a, U−Si and Si−Si bond distances are unrealistically short (1.412(6) and 1.68(1) Å, respectively) and displacement parameters are very high. If the uranium and silicon sites are allowed to freely refine for $U_{1.33}Ni_4Al_8Si_2$, they display an occupancy of 51.6% and 35.6% respectively. The partial occupancy of uranium and, in particular, the very close to one-third occupancy of the silicon site shed light on the true nature of this layer. In this net of U/Si, one-third of the uranium sites are replaced by triangles of three Si atoms, and the silicon sites closest to the remaining uranium atoms are absent. If this is done in an ordered fashion with precisely 67% uranium occupancy and 33% silicon occupancy, a supercell should result with $a' = \sqrt{3}a$, as shown in Figure 4b. This arrangement produces triangles of silicon atoms surrounded by hexagons of uranium; this model yields reasonable U−Si and Si−Si distances of 2.986(4) and 2.45(1)Å, respectively. The U−U distance in this layer is 4.125 Å, which is well above the Hill limit for uranium of 3.5 Å. Below this threshold, the 5f−5f interaction is sufficient to eliminate the uranium magnetic moment leading in some cases to superconductivity; above this distance, the 5f electrons are localized and magnetic ordering can occur.[38] $U_{1.2}Fe_4Si_{9.7}$ and $U_{1-x}Pt_2Al_{7-6x}$ are two other uranium compounds that have been reported with the same

structure type; the former has U−U, U−Si, and Si−Si bond distances of 3.956, 2.883, and 2.30 Å, respectively.[25,27] These are slightly shorter than the corresponding bond distances observed in the $U_{1.33}T_4Al_8Si_2$ structure. Constraining the silicon site to be exactly one-third occupied allowed this position to be refined as a mixture of silicon and gallium, yielding values of 90(1)% Si and 10(1)% Ga on this position. The ordered supercell model mandates a two-thirds occupancy of the uranium site but attempts to constrain the occupancy to this value resulted in high R-values. The freely refined value of 52.6(3)% for the uranium site occupancy is assumed to be correct (since the ordered supercell is not actually observed, see below) and is also in agreement with the uranium content indicated by elemental analysis. The resulting stoichiometry is $U_{1.05}Ni_4Al_{7.72}Si_{1.80}Ga_{0.48}$. The analysis of the cobalt analog indicated similar bond lengths and atomic siting, with the Al1 site having a Al/Ga content of 95(1)%/5(1)%. However, unlike in the Ni analog, the Si site did not show Ga incorporation. The uranium site refined as 67% occupied, closer to the expected occupancy for the supercell; this results in an overall stoichiometry of $U_{1.36}Co_4Al_{7.80}Si_{1.91}Ga_{0.20}$. The idealized stoichiometry $U_{1.33}T_4Al_8Si_2$ will be used for conciseness.

X-ray zone photos were collected on these compounds to further investigate the possible supercell formation; these are shown in Figure 5. The diffraction peaks related to the supercell are much more prominent in the images of the cobalt analog compared to the Ni analog, confirming better ordering
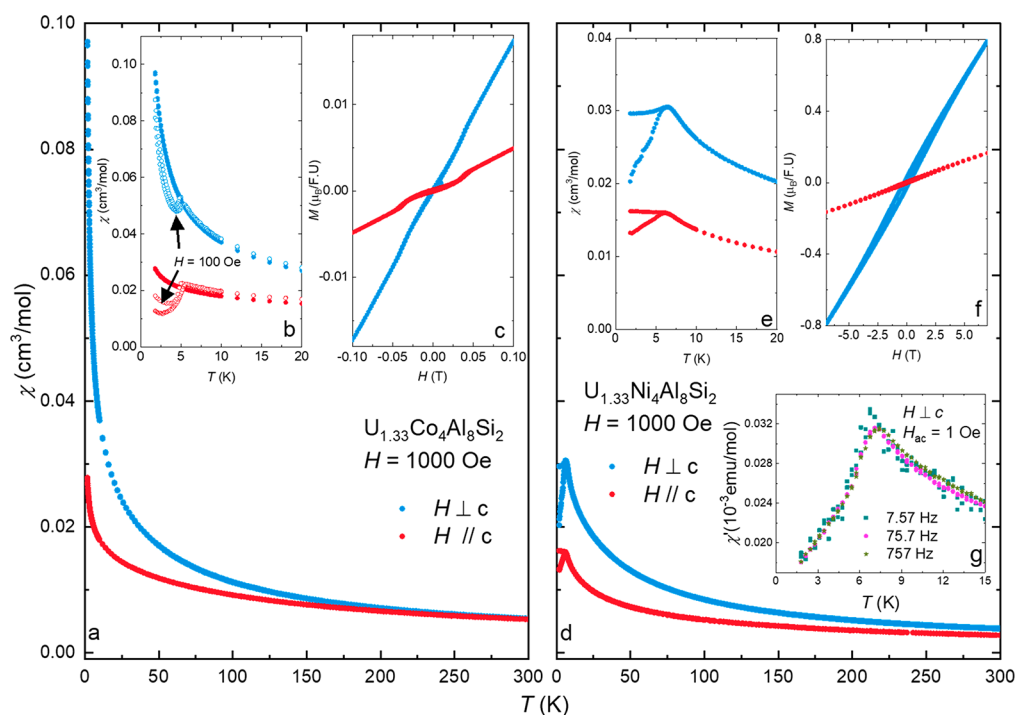
Figure 6. Magnetic susceptibility data for $U_{1.33}Co_4Al_8Si_2$ (left) and $U_{1.33}Ni_4Al_8Si_2$ (right) for magnetic field H applied both parallel and perpendicular to the crystallographic c-axis. (a) $\chi(T)$ for $U_{1.33}Co_4Al_8Si_2$ at 1.8 K < T < 300 K. (b) Same data for 1.8 K < T < 20 K emphasizing the region near magnetic ordering. Note the difference between data collected at 100 and 1000 Oe. (c) $M(H)$ for $U_{1.33}Co_4Al_8Si_2$ at 0 < H < 0.1 T at 1.8 K; above this field range, the magnetization increases linearly up to the maximum field measured (7 T). (d) $\chi(T)$ for $U_{1.33}Ni_4Al_8Si_2$ at 1.8 K < T < 300 K. (e) Same data for 1.8 K < T < 20 K emphasizing the region near magnetic ordering. (f) $M(H)$ for $U_{1.33}Ni_4Al_8Si_2$ at 0 < H < 7 T at 1.8 K. (g) AC magnetic susceptibility $\chi = M/H$ vs temperature T for $U_{1.33}Ni_4Al_8Si_2$ for magnetic field H applied perpendicular to the crystallographic c-axis.

in the U/Si layer in $U_{1.33}Co_4Al_8Si_2$. In addition to disorder in the form of partially occupied sites, the U/Si layer also exhibits stacking disorder, with sequential U/Si layers being shifted out of proper registry along with the a- or b-axes. This is highly prevalent in this structure type. The report on $Ce_2Pt_6Ga_{15}$ included single crystal X-ray diffraction, neutron diffraction, and EXAFS data which pointed to the Ce/Ga layers exhibiting inconsistent positioning.[24] Similar behavior was observed in a TEM and PDF study of $Pr_{1.33}Pt_4Ga_{10}$,[39] and in single crystal studies of $Gd_{0.67}Pt_2Al_4Si$[26] and $Ho_{0.67}Ni_2Ga_{5-x}Ge_x$.[23] The same phenomenon occurs with the $U_{1.33}T_4Al_8Si_2$ title compounds, evidenced by the zone photo data collected on crystals oriented along the b- and c-axis. When aligned along $hk0$, diffraction spots related to the $a' = \sqrt{3}a$ supercell can be observed. However, the $0kl$ zone photo displayed streaks instead of spots demonstrating the lack of stacking order along the c-axis. Additional evidence of the inconsistent positioning of the U/Si layer can be found in the residual electron density map. The highest residual peak in both Ni and Co structures corresponds to where the uranium sites would be if this U/Si layer were rotated 60°. This is likely indicative of some of these layers being out of position, causing the stacking disorder observed along the c-axis. The fact that $U_{1.33}Ni_4Al_8Si_2$ has a comparatively higher value for this peak indicates that it is more disordered than the cobalt analog.

Magnetic Behavior of $U_{1.33}T_4Al_8Si_2$. The combination of disorder, anisotropy, and the quasi-hexagonal planar arrangement of the uranium ions of the $U_{1.33}T_4Al_8Si_2$ structure sets the stage for complex magnetic behavior, as is seen in the magnetic susceptibility χ (Figure 6) for both the Co and Ni variants. For $U_{1.33}Co_4Al_8Si_2$, anisotropic Curie−Weiss paramagnetism occurs at high temperatures where the ab-plane is the easy

direction. Fits to this data yield Weiss constants of $\theta = -107$ and -190 K for fields applied perpendicular ($\perp$) and parallel ($\parallel$) to the crystallographic c-axis, respectively, and magnetic moments per uranium ion of 3.6−3.9 μ_B, consistent with those for other uranium intermetallic compounds such as UBe_{13} and UCd_{11}.[40] These values fall in the overlapping range of moments expected for compounds with trivalent and tetravalent uranium, so the oxidation state of uranium cannot be uniquely identified by this measurement. For the isostructural $U_{1.2}Fe_4Si_{9.7}$ material, the reported magnetic moment per uranium is 2.4 μ_B.[25] Fragile magnetic order which results in an antiferromagnetic-like reduction in the magnetic susceptibility appears at low temperatures, as revealed by comparing $\chi(T)$ measured in applied fields of 100 and 1000 Oe (Figure 6b) and measurements of the magnetization $M(H)$ at $T = 1.8$ K (Figure 6c). In particular, $M(H)$ initially increases linearly, undergoes a subtle increase near $H^* \approx 380$ Oe (particularly for $H \parallel c$), and subsequently increases linearly up to $H = 7$ T. This indicates that there are two distinct magnetic regions that are separated by H^*. The temperature dependence data reinforce this conclusion; while $\chi(T)$ measured at 1000 Oe exhibits a continuous increase to the lowest temperatures, the $\chi(T)$ curves measured at 100 Oe exhibit a sharp reduction near $T_{M,Co} \approx 6$ K. For $H \perp c$, the decrease is followed at lower temperatures by a continuing increase, while for $H \parallel c$, $\chi(T)$ tends to saturate. Furthermore, for both directions, there is field cooled/zero field cooled splitting in $\chi(T)$ and weak hysteresis in $M(H)$ for $H < H^*$. An AC susceptibility study on this compound was uninformative, with no shift of the cusp temperature being observed with different frequencies.
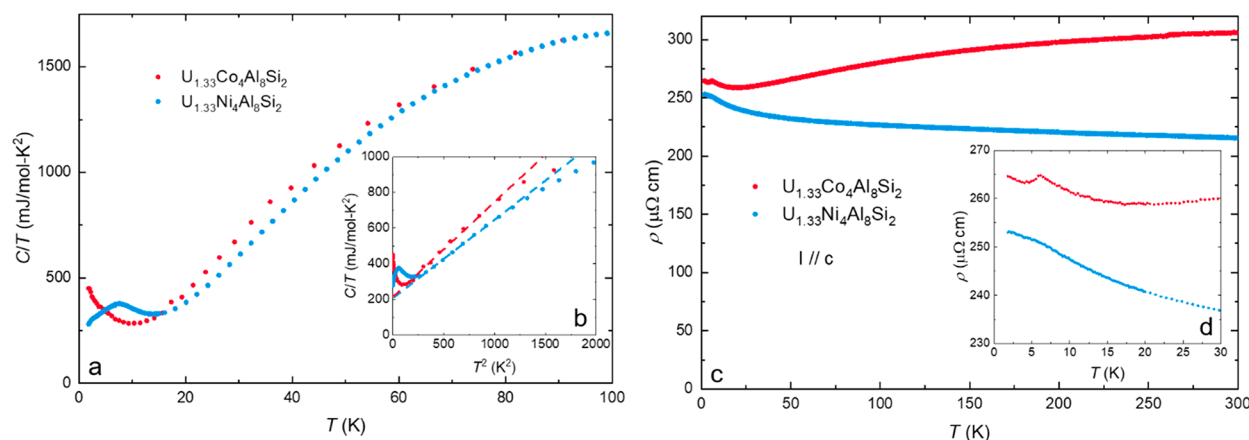
Figure 7. (a) Summary of heat capacity divided by temperature C/T vs temperature T for $U_{1.33}Co_4Al_8Si_2$ and $U_{1.33}Ni_4Al_8Si_2$. (b) C/T vs T^2. The dotted lines are fits to the data using the expression $C/T = \gamma + \beta T^2$, as described in the text. (c) Summary of electrical resistivity ρ vs temperature T for $U_{1.33}Co_4Al_8Si_2$ and $U_{1.33}Ni_4Al_8Si_2$. (d) Results for 1.8 K < T < 20 K, emphasizing the region near magnetic ordering.

Results for the nickel analog $U_{1.33}Ni_4Al_8Si_2$ are summarized in Figure 6d−f. Like the Co-analog, it exhibits Curie−Weiss paramagnetic behavior at high temperature with the *ab*-plane as the easy direction. Fits to the data yield $\theta = −76$ and $−137$ K for $H \perp$ and $\parallel$ to the crystallographic *c*-axis, respectively, and effective magnetic moments per uranium ion between 3.0 and 3.3 μ_B, again consistent with previously reported uranium intermetallic materials.[36] A broad hump is observed in $\chi(T)$ at $T_{M,Ni} \approx 6.1$ K, and splitting of the field-cooled (FC) and zero-field cooled (ZFC) data is seen below this temperature. $M(H)$ curves at 1.8 K are hysteretic and nonsaturating up to 7 T, indicating a remnant moment with weakly ferromagnetic character; however, there is no evidence for a magnetic reconfiguration like that seen in the Co analog. Given the discrepancy between the large negative Weiss constant and the low temperature of the magnetic transition, AC susceptibility measurements were carried out to further explore the ordered state. While a very small shift in the temperature of the cusp is observed with varying frequency (Figure 6g), possibly indicating that the $U_{1.33}Ni_4Al_8Si_2$ is a spin glass material, further studies are needed to characterize this state.

Temperature dependence of heat capacity (C/T vs T) data are shown in Figure 7a. At elevated temperatures, both $U_{1.33}T_4Al_8Si_2$ compounds exhibit similar values, indicating similar lattice terms. Below $T \approx 60$ K, the two curves gradually separate from each other, with the Co compound having an increasingly larger value. The data in the 10−40 K range are described by the Fermi liquid expression $\frac{C_p}{T} = \gamma + \beta T^2$, where γ is the electronic Sommerfeld coefficient and β is the low temperature lattice coefficient. Fits to the data yield $\gamma \approx 210$ mJ/mol-K^2 for both analogs, and $\beta = 0.5$ mJ/mol-K^4 and 0.4 mJ/mol-K^4 for the Co and Ni variants, respectively. The large Sommerfeld coefficients suggest that both compounds are heavy fermion materials, where the charge carrier effective mass is enhanced as a result of the Kondo effect. For isostructural $U_{1.2}Fe_4Si_{9.7}$, γ is 180 mJ mol^{-1}K^{-2}.[25] From the β coefficients, Debye temperatures of 157 and 169 K are estimated for Co and Ni, respectively. Finally, at low temperatures, both data sets deviate from the Fermi liquid expression. $U_{1.33}Ni_4Al_8Si_2$ has a broad peak around $T_{M,Ni} \approx$ 6.5−7 K that is significantly different from the sharp cusps typically denoting long-range magnetic ordering, and $U_{1.33}Co_4Al_8Si_2$ exhibits a gradual upturn than extends to the lowest measured temperatures that likely represents magnetic entropy due to spin fluctuations.

The temperature dependence of the electrical resistivity $\rho(T)$ is presented in Figure 7c, where room temperature values near 200−300 $\mu\Omega$ cm are observed. Both compounds show weak temperature dependences, where $\rho(T)$ gradually decreases and increases for the Co and Ni variants, respectively. At the lowest temperatures the Co variant develops an upturn that is similar to the trend seen for the Ni analogue, and both saturate toward residual resistivity values $\rho_0 \approx 250−275$ $\mu\Omega$cm. The Co and Ni variants have residual resistivity $RRR = \rho_{300 K}/\rho_{1.8K} = 1.15$ and 0.85, respectively. If it is assumed that these materials exhibit metallic or nearly metallic behavior, then the large ρ_0 (and small RRR) values represent disorder scattering of the conduction electrons, as would be expected from the evidence for extensive disorder in the structural refinement of the XRD data. It is also noteworthy that while the Co variant exhibits a cusp near the ordering temperature observed in $\chi(T)$, the Ni variant only shows a broad shoulder. These data support the idea that the phenomena occurring near 6−7 K represent weak ordering or possibly short-range spin glass freezing: e.g., for the Ni analogue, it is sufficient to register in the magnetic susceptibility and heat capacity but not enough to abruptly change the rate at which electrons are scattered.

■ CONCLUSION

Gallium/aluminum mixed metal flux has been found to be a useful medium for the synthesis and crystal growth of complex uranium silicide intermetallics that cannot be synthesized via single-component fluxes or stoichiometric reactions. The $U_{1.33}T_4Al_8Si_2$ products demonstrate excellent stability to air, water, and heat, characteristics crucial to nuclear waste forms. The structural disorder inherent to the $Gd_{1+x}Fe_4Si_{10-y}$ structure type was observed in the title compounds and is reflected in the intricate magnetic properties, with $U_{1.33}Ni_4Al_8Si_2$ displaying likely spin glass behavior, $U_{1.33}Co_4Al_8Si_2$ exhibiting fragile magnetic ordering, and both analogs showing heavy fermion behavior. The $U_{1.33}Co_4Al_8Si_2$ phase exhibits greater evidence of supercell formation compared to the Ni analog, but the ordering was not sufficient to solve the structure in a supercell. In the many analogs of this structure type, two potential ordered supercells have been reported, an orthorhombic cell

and a monoclinic cell.[41,42] The extent of ordering may be dependent on a number of parameters including atom size (as seen here). Further investigation of size effects will be facilitated by the flux growth of analogs with other actinides such as Th and Np. Additional variables that might induce ordering are synthesis procedure (stoichiometric synthesis, arc melting, flux growth), and heating profile (maximum temperature, cooling rate, annealing process). It is notable that the two ordered superstructures were found in compounds grown from reactions with high temperature annealing steps or very slow cooling rates.[41,42] This ordering effect can also be seen in two reports of $Gd_4Pt_9Al_{24}$, a structurally related compound with similar layers of main group triangles and rare earth cations. In both cases the material was grown from an aluminum flux reaction, but one synthesis included a 300 h dwell at 850 °C (yielding a more ordered structure), and the other had a shorter reaction time (producing a disordered/averaged structure).[26,43] It is likely that modification of heating profile will enable control over the extent of ordering in the $R_{1.33}T_4M_{10}$ structure type, and potentially tuning of the magnetic properties of the lanthanides or actinides in this large family of materials.

ASSOCIATED CONTENT

Ⓢ Supporting Information

Crystallographic data in the form of CIF files is available from the CCDC (deposition numbers 1920240 and 1920241). The Supporting Information is available free of charge on the ACS Publications website at DOI: 10.1021/acs.inorgchem.9b01627.

> Microscope images of flux-grown crystals; powder X-ray diffraction patterns for $U_{1.33}T_4Al_8Si_2$ products; thermogravimetric analysis data for $U_{1.33}T_4Al_8Si_2$ products; table of selected bond lengths in the $U_{1.33}T_4Al_8Si_2$ structures; and tables of atom coordinates and atomic percentages of elements in both $U_{1.33}T_4Al_8Si_2$ products (PDF)

Accession Codes

CCDC 1920240−1920241 contain the supplementary crystallographic data for this paper. These data can be obtained free of charge via www.ccdc.cam.ac.uk/data_request/cif, or by emailing data_request@ccdc.cam.ac.uk, or by contacting The Cambridge Crystallographic Data Centre, 12 Union Road, Cambridge CB2 1EZ, UK; fax: +44 1223 336033.

AUTHOR INFORMATION

Corresponding Author

*(S.E.L.) E-mail: latturne@chem.fsu.edu.

ORCID Ⓘ

Susan E. Latturner: 0000-0002-6146-5333

Notes

The authors declare no competing financial interest.

ACKNOWLEDGMENTS

REFERENCES

(1) Schiermeier, Q.; Tollefson, J.; Scully, T.; Witze, A.; Morton, O. Energy alternatives: Electricity without carbon. *Nature* **2008**, *454* (7206), 816−823.

(2) Worrall, A. Utilization of used nuclear fuel in a potential future US fuel cycle scenario. *WM2013*; Phoenix, AZ, 2013.

(3) Bowman, C.; Arthur, E.; Lisowski, P.; Lawrence, G.; Jensen, R.; Anderson, J.; Blind, B.; Cappiello, M.; Davidson, J.; England, T. Nuclear energy generation and waste transmutation using an accelerator-driven intense thermal neutron source. *Nucl. Instrum. Methods Phys. Res. A* **1992**, *320* (1−2), 336−367.

(4) zur Loye, H.-C.; Besmann, T.; Amoroso, J.; Brinkman, K.; Grandjean, A.; Henager, C. H.; Hu, S.; Misture, S. T.; Phillpot, S. R.; Shustova, N. B.; Wang, H.; Koch, R. J.; Morrison, G.; Dolgopolova, E. Hierarchical Materials as Tailored Nuclear Waste Forms: A Perspective. *Chem. Mater.* **2018**, *30* (14), 4475−4488.

(5) Quapp, W. J.; Lessing, P. A. *Radiation shielding composition*. US 6,166,390A, 1998.

(6) Dole, L. R.; Quapp, W. Radiation shielding using depleted uranium oxide in nonmetallic matrices. *ORNL/TM-2002/111*; Oak Ridge National Laboratory, UT-Battelle, LLC: Oak Ridge, TN, 2002.

(7) Mattus, C.; Dole, R. Durability of depleted uranium aggregates in ducrete shielding applications. In *The 10th International Conference on Environmental Remediation and Radioactive Waste Management*, September 4−8, 2005, Scottish Exhibition & Conference Centre: 2005.

(8) Nozariasbmarz, A.; Agarwal, A.; Coutant, Z. A.; Hall, M. J.; Liu, J.; Liu, R.; Malhotra, A.; Norouzzadeh, P.; Öztürk, M. C.; Ramesh, V. P. Thermoelectric silicides: A review. *Jpn. J. Appl. Phys.* **2017**, *56* (5S1), 05DA04.

(9) Samsonov, G. V. The chemistry of the silicides of the rare-earth elements. *Russ. Chem. Rev.* **1962**, *31* (12), 702−712.

(10) Schlesinger, M. E. Thermodynamics of solid transition-metal silicides. *Chem. Rev.* **1990**, *90* (4), 607−628.

(11) Hsu, C.-C. Formation of Rare Earth Metal Silicides. *Surface Physics And Related Topics: Festschrift for Xie Xide* **1991**, 194−212.

(12) Chełmicki, L.; Leciejewicz, J.; Zygmunt, A. Magnetic properties of UT_2Si_2 and UT_2Ge_2 (T= Co, Ni, Cu) intermetallic systems. *J. Phys. Chem. Solids* **1985**, *46* (5), 529−538.

(13) Matsuda, T. D.; Haga, Y.; Ikeda, S.; Galatanu, A.; Yamamoto, E.; Shishido, H.; Yamada, M.; Yamaura, J.-I.; Hedo, M.; Uwatoko, Y. Electrical and magnetic properties of a single crystal UCu_2Si_2. *J. Phys. Soc. Jpn.* **2005**, *74* (5), 1552−1556.

(14) Palstra, T.; Menovsky, A.; Van den Berg, J.; Dirkmaat, A.; Kes, P.; Nieuwenhuys, G.; Mydosh, J. Superconducting and Magnetic Transitions in the Heavy-Fermion System URu_2Si_2. *Phys. Rev. Lett.* **1985**, *55* (24), 2727.

(15) Sandratskii, L.; Kübler, J. Inferred physical properties of UT_2Si_2 (T= Ru, Rh, Pd) from spin-density functional calculations. *Solid State Commun.* **1994**, *91* (3), 183−186.

(16) Matsuda, T. D.; Metoki, N.; Haga, Y.; Ikeda, S.; Okubo, T.; Sugiyama, K.; Nakamura, N.; Kindo, K.; Kaneko, K.; Nakamura, A. Single crystal growth and structural and magnetic properties of the uranium ternary intermetallic compound UCr_2Si_2. *J. Phys. Soc. Jpn.* **2003**, *72* (1), 122−130.

(17) Canepa, F.; Manfrinetti, P.; Pani, M.; Palenzona, A. Structural and transport properties of some UTX compounds where T = Fe, Co, Ni and X = Si, Ge. *J. Alloys Compd.* **1996**, *234* (2), 225−230.

(18) Kanatzidis, M. G.; Pöttgen, R.; Jeitschko, W. The metal flux: a preparative tool for the exploration of intermetallic compounds. *Angew. Chem., Int. Ed.* **2005**, *44* (43), 6996−7023.

(19) Latturner, S. E. Clusters, Assemble: Growth of Intermetallic Compounds from Metal Flux Reactions. *Acc. Chem. Res.* **2018**, *51* (1), 40−48.

(20) Phelan, W. A.; Menard, M. C.; Kangas, M. J.; McCandless, G. T.; Drake, B. L.; Chan, J. Y. Adventures in crystal growth: synthesis and characterization of single crystals of complex intermetallic compounds. *Chem. Mater.* **2012**, *24* (3), 409−420.

(21) Benavides, K. A.; Oswald, I. W.; Chan, J. Y. Casting a Wider Net: Rational Synthesis Design of Low-Dimensional Bulk Materials. *Acc. Chem. Res.* **2018**, *51* (1), 12−20.

(22) Latturner, S.; Bilc, D.; Mahanti, S.; Kanatzidis, M. G. Quaternary Intermetallics Grown from Molten Aluminum: The Homologous Series $Th_2(Au_xSi_{1-x})[AuAl_2]_nSi_2$ (n= 1, 2, 4). *Chem. Mater.* **2002**, *14* (4), 1695−1705.

(23) Zhuravleva, M. A.; Chen, X.; Wang, X.; Schultz, A. J.; Ireland, J.; Kannewurf, C. K.; Kanatzidis, M. G. X-ray and Neutron Structure Determination and Magnetic Properties of New Quaternary Phases $RE_{0.67}Ni_2Ga_{5+n-x}Ge_x$ and $RE_{0.67}Ni_2Ga_{5+n-x}Si_x$ (n= 0, 1; RE= Y, Sm, Gd, Tb, Dy, Ho, Er, Tm) Synthesized in Liquid Ga. *Chem. Mater.* **2002**, *14* (7), 3066−3081.

(24) Kwei, G.; Lawson, A.; Larson, A.; Morosin, B.; Larson, E.; Canfield, P. Structure of $Ce_2Pt_6Ga_{15}$: interplanar disorder from the Ce_2Ga_3 layers. *Acta Crystallogr., Sect. B: Struct. Sci.* **1996**, *52* (4), 580−585.

(25) Noguchi, S.; Okuda, K.; Abliz, M.; Goto, K.; Kindo, K.; Haga, Y.; Yamamoto, E.; Ōnuki, Y. High field magnetization of the new heavy fermion compound $U_{1.2}Fe_4Si_{9.7}$. *Phys. B* **1998**, *246−247*, 456−459.

(26) Latturner, S.; Kanatzidis, M. G. $Gd_{1.33}Pt_3(Al, Si)_8$ and $Gd_{0.67}Pt_2(Al, Si)_5$: Two structures containing a disordered Gd/Al layer grown in liquid aluminum. *Inorg. Chem.* **2002**, *41* (21), 5479−5486.

(27) Bobev, S.; Bauer, E. D.; Sarrao, J. L. Uranium and aluminium order−disorder in $U_{1-x}Pt_2Al_{7-6x}$ [x= 0.33 (1)]. *Acta Crystallogr., Sect. E: Struct. Rep. Online* **2006**, *62* (4), i77−i79.

(28) Niermann, J.; Jeitschko, W. Ternary Aluminides with the Ideal Composition $A_2Pt_6Al_{15}$ (A = Y, Gd—Tm, Zr). *Z. Anorg. Allg. Chem.* **2004**, *630*, 361−368.

(29) Hooft, R. *COLLECT*; Nonius BV: Delft, The Netherlands, 1996.

(30) Sheldrick, G. *APEX II*; Bruker-AXS: Madison, WI, 1998.

(31) Sheldrick, G. M. A short history of SHELX. *Acta Crystallogr., Sect. A: Found. Crystallogr.* **2008**, *64* (1), 112−122.

(32) Sieve, B.; Gray, D. L.; Henning, R.; Bakas, T.; Schultz, A. J.; Kanatzidis, M. G. Al flux synthesis of the oxidation-resistant quaternary phase $REFe_4Al_9Si_6$ (RE= Tb, Er). *Chem. Mater.* **2008**, *20* (19), 6107−6115.

(33) Potter, W. M.; Lai, Y.; Cao, H.; Baumbach, R. E.; Latturner, S. E. $U_8Al_{19}Si_6$, A Uranium Aluminide Silicide with a Stuffed Supercell Grown from Aluminum Flux. *Chem. Mater.* **2018**, *30*, 3806−3812.

(34) Chen, X.-Z.; Sieve, B.; Henning, R.; Schultz, A. J.; Brazis, P.; Kannewurf, C. R.; Cowen, J. A.; Crosby, R.; Kanatzidis, M. G. $Ln_2Al_3Si_2$ (Ln = Ho, Er, Tm): New Silicides from Molten Aluminum—Determination of the Al/Si Distribution with Neutron Crystallography and Metamagnetic Transitions. *Angew. Chem., Int. Ed.* **1999**, *38*, 693−696.

(35) Sieve, B.; Chen, X.; Henning, R.; Brazis, P.; Kannewurf, C.; Cowen, J.; Schultz, A.; Kanatzidis, M. G. Cubic Aluminum Silicides $RE_8Ru_{12}Al_{49}Si_9$ (Al_xSi_{12-x})(RE= Pr, Sm) from Liquid Aluminum. Empty (Si, Al) 12 Cuboctahedral Clusters and Assignment of the Al/Si Distribution with Neutron Diffraction. *J. Am. Chem. Soc.* **2001**, *123*, 7040−7047.

(36) Gladyshevskii, R.; Cenzual, K.; Flack, H.; Parthé, E. Structure of RNi_3Al_9 (R= Y, Gd, Dy, Er) with either ordered or partly disordered arrangement of Al atom triangles and rare earth metal atoms. *Acta Crystallogr., Sect. B: Struct. Sci.* **1993**, *49* (3), 468−474.

(37) Zhuravleva, M. A.; Kanatzidis, M. G. Molten Gallium as a Non-Reactive Solvent: Synthesis of the Silicides $RE_2Ni_{3+x}Si_{5-x}$ (RE = Sm, Gd and Tb). *Z. Naturforsch., B: J. Chem. Sci.* **2003**, *58b*, 649−657.

(38) Hill, H. In *Plutonium 1970 and other actinides*; Miner, W. N., Ed.; AIME: New York, 1970; p 2.

(39) Doan Nguyen, S.; Ryan, K.; Chai, P.; Shatruk, M.; Xin, Y.; Chapman, K. W.; Chupas, P. J.; Fronczek, F. R.; Macaluso, R. T. $Pr_{1.33}Pt_4Ga_{10}$: Superstructure and magnetism. *J. Solid State Chem.* **2014**, *220*, 9−16.

(40) Stewart, G. R. Heavy-fermion systems. *Rev. Mod. Phys.* **1984**, *56* (4), 755−787.

(41) Prots, Y.; Deppe, M.; Cardoso-Gil, R.; Cervellino, A.; Ormeci, A.; Geibel, C.; Grin, Y. $Yb_2Al_{15}Pt_6$ − the most ordered variety of the $Sc_{1.2}Fe_4Si_{9.8}$ aristotype. *Chem. Met. Alloys* **2014**, No. 7, 85−99.

(42) Radziewski, M.; Stegemann, F.; Hoffmann, R.-D.; Janka, O. The monoclinic superstructure of the $M_2Pt_6Al_{15}$ series (M= Ca, Sc, Y, La, Lu). *Z. Kristallogr. - Cryst. Mater.* **2017**, *232* (10), 675−687.

(43) Thiede, V. M.; Fehrmann, B.; Jeitschko, W. Ternary rare earth metal palladium and platinum aluminides $R_4Pd_9Al_{24}$ and $R_4Pt_9Al_{24}$. *Z. Anorg. Allg. Chem.* **1999**, *625* (9), 1417−1425.